

Jet-torus connection in radio galaxies

Relativistic hydrodynamics and synthetic emission

C. M. Fromm^{1,2}, M. Perucho^{3,4}, O. Porth¹, Z. Younsi¹, E. Ros^{2,3,4}, Y. Mizuno¹, J. A. Zensus² and L. Rezzolla^{1,5}

¹ Institut für Theoretische Physik, Goethe Universität, Max-von-Laue-Str. 1, D-60438 Frankfurt, Germany

² Max-Planck-Institut für Radioastronomie, Auf dem Hügel 69, D-53121 Bonn, Germany

³ Departament d'Astronomia i Astrofísica, Universitat de València, Dr. Moliner 50, E-46100 Burjassot, València, Spain

⁴ Observatori Astronòmic, Parc Científic, Universitat de València, C/ Catedràtic José Beltrán 2, E-46980 Paterna, València, Spain

⁵ Frankfurt Institute for Advanced Studies, Ruth-Moufang-Strasse 1, 60438 Frankfurt, Germany e-mail: cfromm@th.physik.uni-frankfurt.de

Preprint online version: March 8, 2018

ABSTRACT

Context. High-resolution Very-Long-Baseline Interferometry observations of active galactic nuclei have revealed asymmetric structures in the jets of radio galaxies. These asymmetric structures may be due to internal asymmetries in the jet, could be induced by the different conditions in the surrounding ambient medium including the obscuring torus, or a combination of the two.

Aims. In this paper we investigate the influence of the ambient medium (including the obscuring torus) on the observed properties of jets from radio galaxies.

Methods. We performed special-relativistic hydrodynamic (RHD) simulations of over-pressured and pressure-matched jets using the special-relativistic hydrodynamics code *Ratpenat*, which is based on a second-order accurate finite-volume method and an approximate Riemann solver. Using a newly developed emission code to compute the electromagnetic emission, we have investigated the influence of different ambient medium and torus configurations on the jet structure and subsequently computed the non-thermal emission produced by the jet and the thermal absorption due to the torus. To better compare the emission simulations with observations we produced synthetic radio maps, taking into account the properties of the observatory.

Results. The detailed analysis of our simulations shows that the observed asymmetries can be produced by the interaction of the jet with the ambient medium and by the absorption properties of the obscuring torus.

Key words. galaxies: active, – galaxies: jets, – radio continuum: galaxies, – radiation mechanisms: non-thermal

1. Introduction

Active galactic nuclei (AGN) are generally assumed to consist of a central, compact massive object (i.e., a supermassive black hole), an accretion disk surrounded by a molecular torus, and a jet launched perpendicular to the black-hole disk system. Within this standard model, AGN may be classified according to their orientation with respect to the line of sight. If the AGN is seen at a viewing angle of $\vartheta = 90^\circ$ (i.e., edge-on), the innermost regions are obscured by the torus and more internal features become observable as the viewing angle decreases (Antonucci 1993; Urry & Padovani 1995).

In addition to the classification of AGN by their viewing angle, Fanaroff & Riley (1974) introduced a division based on the morphology of the jets themselves: Fanaroff-Riley I (FR I) jets are characterised by a bright core and FR II jets are dominated by their bright lobes.

The large-scale structure of AGN observed at high viewing angles can be resolved through radio interferometric observations (see, e.g., Kharb et al. 2008) and high resolution very-long-baseline interferometry (VLBI) observations enable us to probe its morphological evolution on parsec scales (see, e.g., Lister et al. 2009). These jets remain collimated over long distances, up to kilo-parsec scales, at which they can be modelled using special-relativistic (magneto-)hydrodynamical [R(M)HD] simulations and the computed emission and polarisation properties provide insights into the underlying fluid properties and mag-

netic field configurations (see, e.g., Perucho & Martí 2007; Laing & Bridle 2002; Hardcastle & Krause 2013).

In the infrared band, the electromagnetic emission from these AGN is assumed to be generated by the re-emission by the obscuring torus of the radiation initially produced in the accretion disc. Based on observations, two kinds of torus model were constructed, namely smooth torus models and clumpy torus models (for a review of torus models see, e.g., Hoenig 2013).

So far both models have been applied successfully to explain observational results either at kilo-parsec scales (via jet simulations) or at sub-parsec scales (via torus simulations). However, to explain the VLBI observations of AGN viewed almost edge-on ($\vartheta \sim 90^\circ$), both a jet model and a torus model should be included. In this paper we combine both approaches, addressing the question of the impact that the combination of the torus and of the ambient medium have on the observed properties of the jet at parsec scales.

Additionally, we aim to make the connection between numerical simulations of relativistic outflows and their emission with observations in a deeper way than has been done so far. Jet acceleration, re-collimation, and other phenomena have been understood with the help of one-dimensional (1D), 2D, and 3D numerical simulations, including different ingredients such as magnetic fields and special relativity (see, e.g., Mizuno et al. 2015). Some emission codes have even been applied (Gómez et al. 1997; Mimica et al. 2009) to explain the emission. Here we

go one step further and consider additional components in the AGN picture, such as the obscuring torus, and including time-delays, emission and absorption in a code which will enable us to compare with real observations of two-sided sources in future works.

The organisation of the paper is as follows. In Sec. 2 we introduce our numerical setup for the jet and the torus. The results of the simulations and the emission calculations are presented in Sects. 3.1–3.2. The discussion of our results is provided in Sec. 4. Throughout the paper we assume an ideal-fluid equation of state $p = \rho\epsilon(\hat{\gamma} - 1)$, where p is the pressure, ρ the rest-mass density, ϵ the specific internal energy, and $\hat{\gamma}$ the adiabatic index (Rezzolla & Zanotti 2013).

2. RHD Simulations

We performed several 2D axisymmetric simulations of supersonic special-relativistic hydrodynamical jets using the finite-volume code Ratpenat (for more details see Perucho et al. 2010, and references therein).

2.1. Jet model

The numerical setup is similar to the one used in Fromm et al. (2016) and for completeness we provide below a short summary.

The numerical grid consisted of 320 cells in the radial direction and 400 cells in the axial direction. Using a numerical resolution of 4 cells per jet radius (R_j), the grid covered $80 R_j \times 100 R_j$. We assume the z axis to be in the direction of propagation of the jet and the x axis to represent the radial cylindrical coordinate. The boundary conditions were reflection at the jet axis, injection at the jet nozzle and outflow conditions elsewhere. We filled the simulation box with a jet and the parameters used were: the velocity of the jet v_b , the bulk Lorentz factor Γ , the classical Mach number of the jet M , the rest-mass density of the jet ρ_b , and the adiabatic index $\hat{\gamma}$. The pressure, p_b at the jet nozzle was computed from the Mach number using an ideal-fluid equation of state. The ratio $d_k = p_b/p_a$ between the pressure in the jet, p_b , and the pressure in the ambient medium, p_a , led to a pressure matched (PM) jet (i.e., with $d_k = 1$) or to an over-pressured (OP) jet (i.e., with $d_k > 1$). Depending on this ratio, internal structures in the jet, the so-called recollimation shocks, were formed in the case of an OP jet or the jet appeared featureless in the case of a PM jet (Mizuno et al. 2015). The properties of the ambient medium (e.g., the gradient in the ambient pressure and ambient rest-mass density) played a crucial role on the shape of the jet and on the properties of the created recollimation shocks in the case of OP jets. We modelled the decrease in the ambient medium pressure using a pressure profile presented in Gómez et al. (1997) as

$$p_a(z) = \frac{p_b}{d_k} \left[1 + \left(\frac{z}{z_c} \right)^n \right]^{-\frac{m}{n}}, \quad (1)$$

where z_c can be considered as the core radius and the exponents n and m control the steepening of the ambient pressure. The initial conditions, given in code units (speed of light $c = 1$, jet radius R_j , and ambient medium rest-mass density, $\rho_a = 1 \text{ g cm}^{-3}$) are listed in Table 1

The distributions of the ambient pressure and of the ambient rest-mass density for the parameters for the jet models considered here is shown in Fig. 1. Throughout the paper we used a single value of $n = 1.5$, while setting $m = 2, 3, 4$.

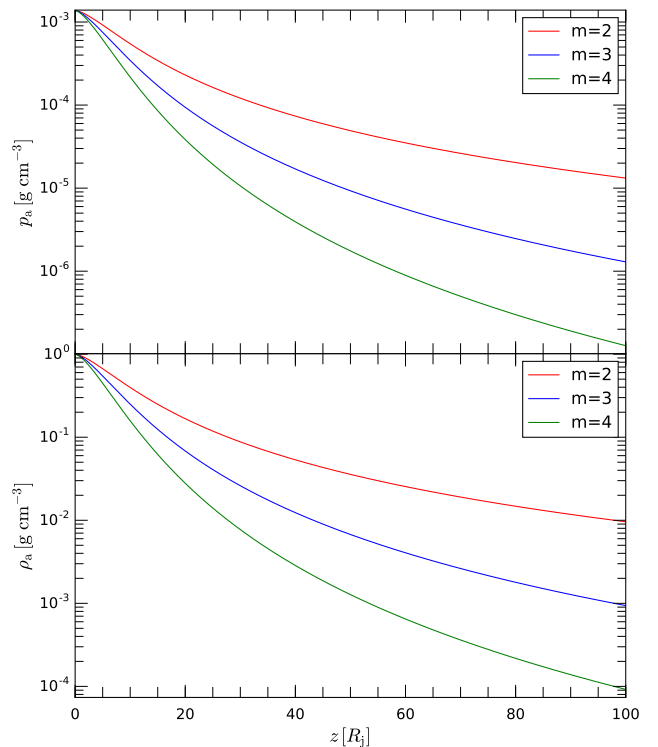


Fig. 1. Distribution of the ambient pressure and the ambient rest-mass density in code units for the gradients in the ambient medium

Table 1. Initial parameters for the jet.

Model	R_b [R_j]	v_b	d_k	Γ	ρ_b [g cm^{-3}]	M	$\hat{\gamma}$
PM	1	0.5	1.0	1.15	0.04	1.6	13/9
OP	1	0.5	2.5	1.15	0.04	1.6	13/9

2.2. Torus model

Once a stationary state for the jet was reached, typically after 5 grid longitudinal crossing times, we inserted a steady-state torus. We assumed that the torus did not influence the dynamics of the jet and therefore the torus should be regarded as a phenomenological model; we refer the reader to Stalevski et al. (2016) for a detailed discussion of the torus modelling.

More specifically, our torus model is adapted from Stalevski et al. (2012, 2016) and the geometry of the torus can be seen in Fig. 2. The geometry of the model resembles a “flared disk” and is characterised by three parameters: the inner radius of the torus, R_{in} , the outer radius of the torus, R_{out} and the half-opening angle Θ . For the inner radius of the torus we used

$$\left(\frac{R_{\text{in}}}{\text{pc}} \right) \approx 1.3 \left(\frac{L_{\text{AGN}}}{10^{46} \text{ erg s}^{-1}} \right)^{0.5} \left(\frac{T_{\text{sub}}}{1500 \text{ K}} \right)^{-2.8}, \quad (2)$$

where L_{AGN} is the bolometric luminosity and T_{sub} is the sublimation temperature of the dust grains. We assumed a power law distribution for the rest-mass density in the torus, given by

$$\rho = \rho(R_{\text{in}}) \left(\frac{r}{R_{\text{in}}} \right)^{-k} e^{-l|\cos\Theta|}, \quad (3)$$

where the $\cos\Theta$ -dependence in the Eq. (3) leads to a concentration of rest-mass density towards the equatorial plane. Since we

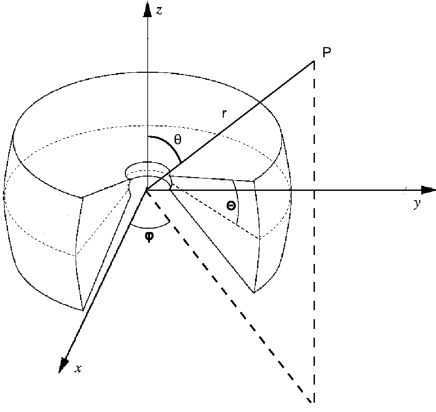


Fig. 2. Geometry of the assumed torus model (adapted from Stalevski et al. 2012).

do not perform a radiative modelling of the torus, its temperature distribution is simply assumed to follow a certain prescription. In particular, following Schartmann et al. (2005), the temperature decrease moving outwards in the radial direction; furthermore, because of the direct illumination of the inner torus walls, the temperature should decrease when going from high to low latitudes. Such behaviour may be modelled with the following temperature profile

$$T = T_{\text{sub}} \left(\frac{r}{R_{\text{in}}} \right)^{-k} e^{-l|\sin(\Theta-\theta)|}. \quad (4)$$

Figure 3 illustrates the distribution of the temperature and of the rest-mass density in the torus with $L_{\text{AGN}} = 10^{43} \text{ erg s}^{-1}$, $T_{\text{sub}} = 1500 \text{ K}$, which leads to an inner radius of $R_{\text{in}} = 4 R_j$. The outer radius is set to $R_{\text{out}} = 30 R_j$ and the angular thickness of the torus is $\theta = 50^\circ$. For the scaling of the rest-mass density we have set $\rho(R_{\text{in}}) = 1.6 \times 10^{-20} \text{ g cm}^{-3}$, while the exponents for the distribution of the temperature and rest-mass density are $k = 1$ and $l = 2$.

3. Results

3.1. Relativistic Hydrodynamics

In Fig. 4 we show the 2D distribution of the rest-mass density of the stationary jets from our (RHD) simulations. Each panel corresponds to a different ambient medium configuration as characterised by the exponent m [see Eq. (1)]. The left-half of each panel ($-30 < r/R_j < 0$) shows the distribution for the OP jet and the right-half of each panel ($0 < r/R_j < 30$) for the PM jet. The upper row presents the entire simulation grid and the lower row a magnified view of the nozzle region of the jets ($0 < z/R_j < 7$).

In the case of OP jets, the initial pressure mismatch at the nozzle led to the generation of two shock waves: one travelling radially outward and the other propagating inwards in the direction of the jet axis. Between these two shocks the jet radially expanded until a pressure equilibrium with the ambient medium was reached. This equilibrium is first obtained at the jet-ambient medium boundary and leads to an inward travelling wave (indicated by the bold dashed lines in the bottom row of Fig. 4). The radial expansion of the jet is stopped as soon as the expansion regions are crossed by the inward travelling sound waves. Since these waves propagate with the local sound speed, the outer regions in the jet already stop expanding while the inner

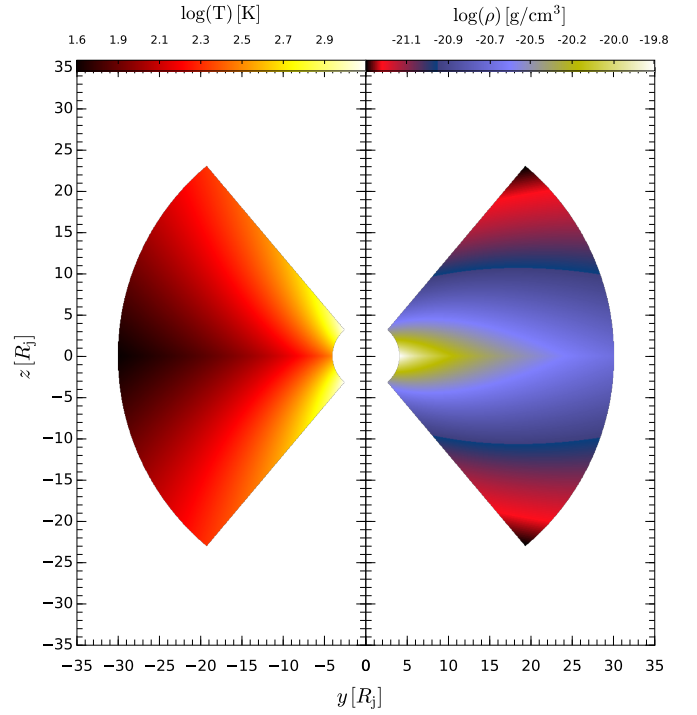


Fig. 3. Left panel: distribution of temperature in the meridional plane. Right panel: corresponding rest-mass density distribution. The Θ -dependence in the distribution of the temperature and the rest-mass density is clearly visible.

regions continue to expand (further decreasing the pressure and rest-mass density). The innermost region in the jet stops expanding as soon as the sound wave reaches the jet axis. At this position, a recollimation shock is formed, which can be regarded as a new jet nozzle (local maximum in pressure and rest-mass density) and so the flow expands again (see e.g., Daly & Marscher 1988; Falle 1991; Mizuno et al. 2015). The recollimation shocks are clearly visible at $z \sim 6 R_j$ in the upper-half of the panels in the left column of Fig. 4. At the position of the recollimation shock, a new radially outward travelling wave is formed and the jet expands again.

If the gradient in the ambient medium at the position of the first recollimation shock ($z \sim 6 R_j$) is steep enough, the sound waves reflected from the boundary between the jet and the ambient medium (generated after reaching radial pressure equilibrium) cannot reach the jet axis and therefore no additional recollimation shock is formed and the jet continues to expand (for detailed discussion see Porth & Komissarov 2015). With our settings for the ambient medium this behaviour is obtained for models with $m > 2$. In these cases, even for the OP jets no additional recollimation shocks are formed beyond $z_c \sim 6 R_j$ and a conical jet shape is obtained further downstream.

In contrast to the OP jets, in PM jets there is a radial-pressure equilibrium at the nozzle. Therefore, only minor variations were created within the jet and the pressure and rest-mass density were continuously decreasing (except for $m = 4$ which triggered a shock at $z \sim 60 R_j$). The opening angle of these jets depends on the gradient in the ambient medium: the steeper the gradient the larger the opening angle of the jet. This behaviour is visible in the first column of Fig. 4.

A detailed picture of the influence of the pressure ratio at the jet nozzle, d_k , and the configuration of the ambient medium on the shape of the jet and its fluid parameters can be obtained

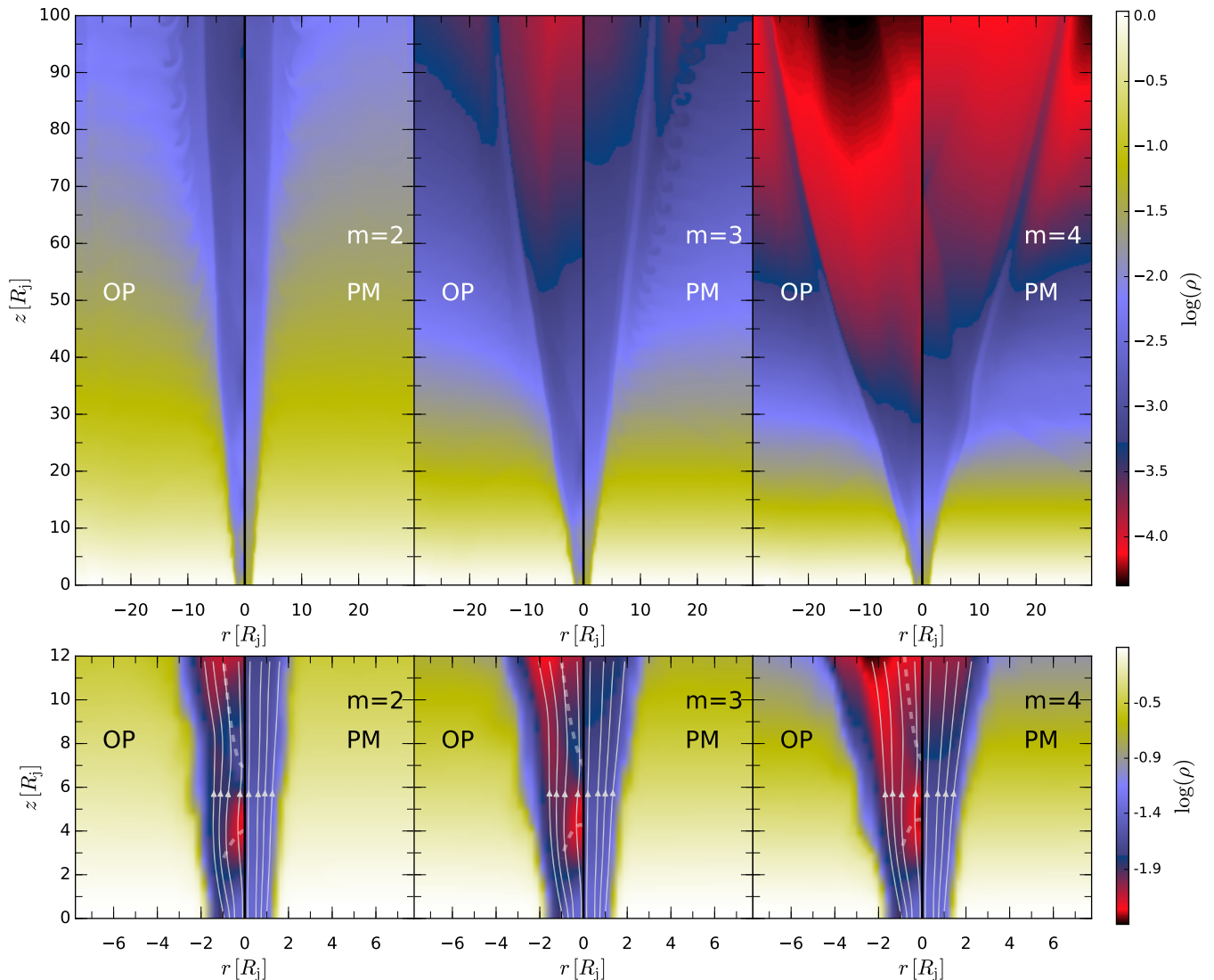


Fig. 4. Stationary results for the jet simulations. The panels show the 2D distribution of the rest-mass density for different ambient medium configurations as indicated by the exponent m . In each panel the left part ($-30 < r/R_j < 0$) corresponds to the OP jet and the right part ($0 < r/R_j < 30$) to the PM jet. The upper row spans the entire simulation grid whereas the bottom row shows a magnified view of the nozzle region ($-7 < z/R_j < 7$). The white lines in the bottom row show stream lines visualising the direction of the flow and the bold dashed lines correspond to the inward travelling and reflected shock wave.

by analysing their evolution along the jet axis. The variation of the normalised jet radius r/R_j , of the axial pressure p_{axial} , and of the axial velocity v_{axial} , for the different jet and ambient medium models is shown in Fig. 5. The largest variations in the jet parameters occur at small scales (i.e., for $z \lesssim 20 R_j$) and for different jet models, i.e., pressure matched or over-pressured. Within a jet model the modification of the gradient in the ambient medium leads to variations, but not to a different evolution of the parameters along the jet axis.

In the case of PM jets, stronger gradients in the ambient medium led to larger jet radii, r , faster velocities, v_{axial} , and smaller axial pressures, p_{axial} . This behaviour can be understood in the following way: The radial position where a pressure equilibrium between the jet and the ambient medium is reached (given the same initial pressure at the jet nozzle) shifts downstream with the gradient in the ambient medium. Since the jet is in pressure equilibrium with the ambient medium, the axial pres-

sure in the jet is equal to the pressure in the ambient medium, so that the steeper the gradient in the ambient medium the stronger the decrease in the jet pressure. According to the conservation equations of hydrodynamics, a hot supersonic flow accelerates if its cross section increases (Rezzolla & Zanotti 2013); thus a PM jet embedded in an ambient medium with larger gradients (hence larger jet radii) develops higher velocities as the same jet surrounded by an ambient medium with smaller gradients (see bottom panel of Fig. 5).

In contrast to the smooth evolution of the jet parameters (r , p_{axial} , and $v_{z,\text{axial}}$) for the PM jet, large variations are present in the parameters for OP jets (see Fig. 5). As already mentioned the initial pressure-mismatch at the jet nozzle leads to an opening of the jet and as soon as a radial pressure equilibrium was reached a radially inward travelling wave was formed. The larger the gradient in the ambient medium, the larger the jet radii where the pressure equilibrium was obtained became. Due to the finite

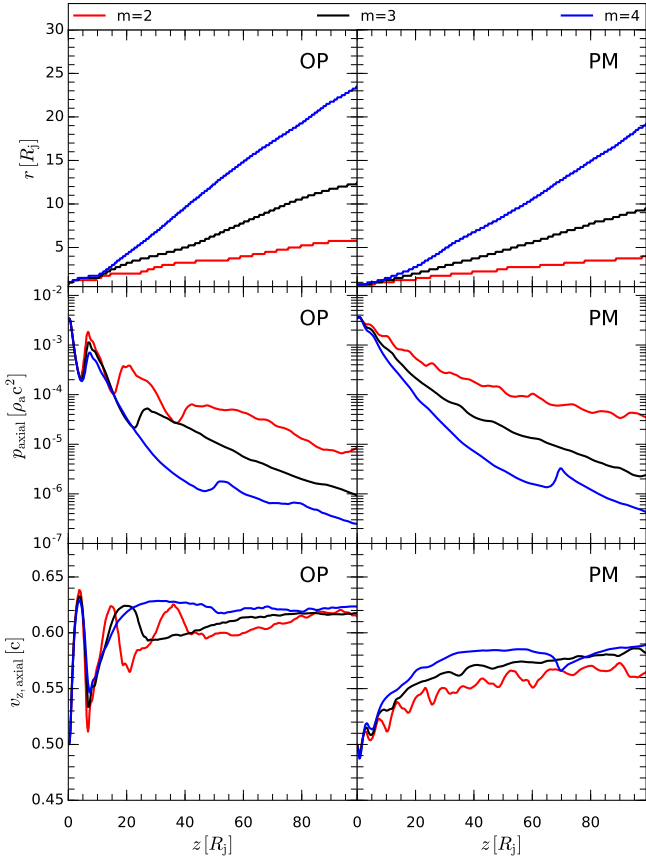


Fig. 5. Variation of the jet parameters along the jet axis. The left column corresponds to OP jets and right one to PM jets. From top to bottom: jet radius, axial pressure and axial velocity in the z -direction (see text for details).

sound speed, the crossing time of this wave increased with jet radius. The inner parts of the jet stopped expanding as soon as the sound wave crossed the jet axis. Therefore, the pressure decreased for larger jet radii i.e., a steeper gradient in the ambient medium (compare solid red and blue lines in the middle panel of Fig. 5).

After the sound wave crossed the jet axis, the pressure increased to values comparable with the pressure in the ambient medium (see middle panel of Fig. 5 at $z \sim 8 R_j$). The difference in position of the pressure jump and its magnitude reflects the difference in the sound crossing time and the gradient in the ambient medium. Since the OP jets exhibit larger jet radii than PM jets, the fluid is accelerated to higher velocities, $v_{z,\text{axial}}$ at $z \sim 5 R_j$. The formation of the recollimation shock at $z \sim 6 R_j$ leads to a sharp decrease in the axial velocity $v_{z,\text{axial}}$, and the expansion of the fluid after crossing the recollimation shock leads to an increase in the axial velocity. After $z > 10 R_j$, the rapid decrease in the ambient-medium pressure induces an expansion of the jet, which is accompanied by a decrease in the jet pressure, p_{axial} , and a slight increase in the axial jet velocity. In the case of the smallest gradients in the ambient medium ($m = 2$) additional recollimation shocks are formed at $z \sim 20$ and at $z \sim 40$ (see the solid red curve in Fig. 5).

3.2. Emission

For the calculation of the emission we follow the methods described in Gómez et al. (1997) and Mimica et al. (2009). For completeness we provide here the basic equations and underlying assumptions for the calculation of non-thermal emission. We assumed a power law distribution of relativistic electrons

$$n(\gamma_e) = n_0 \left(\frac{\gamma_e}{\gamma_{e,\text{min}}} \right)^{-s} \quad \text{for } \gamma_{e,\text{min}} \leq \gamma_e \leq \gamma_{e,\text{max}}, \quad (5)$$

where n_0 is a normalisation coefficient, γ is the electron Lorentz factor, γ_{min} and γ_{max} are the lower and upper electron Lorentz factors and s is the spectral slope. In order to construct the distribution of non-thermal particles from the thermal population we assumed that the number density of relativistic particles is a fraction ζ_e of the thermal particles

$$\int_{\gamma_{e,\text{min}}}^{\gamma_{e,\text{max}}} n(\gamma_e) d\gamma = \zeta_e \frac{\rho}{m_p}, \quad (6)$$

where m_p is the proton mass. The second assumption relates the energy in the relativistic particles to the energy in the thermal particles via the parameter ϵ_e as follows

$$\int_{\gamma_{e,\text{min}}}^{\gamma_{e,\text{max}}} n(\gamma_e) \gamma_e m_e c^2 d\gamma = \epsilon_e \frac{p}{\hat{\gamma} - 1}, \quad (7)$$

where m_e is the electron mass. After performing the integration in Eq. (6) and Eq. (7) a relation for lower electron Lorentz factor, $\gamma_{e,\text{min}}$, may be derived as

$$\gamma_{e,\text{min}} = \begin{cases} \frac{p}{\rho} \frac{m_p}{m_e c^2} \frac{(s-2)}{(s-1)(\hat{\gamma}-1)} \frac{\epsilon_e}{\zeta_e} & \text{if } s > 2, \\ \left[\frac{p}{\rho} \frac{m_p}{m_e c^2} \frac{(2-s)}{(s-1)(\hat{\gamma}-1)} \frac{\epsilon_e}{\zeta_e} \gamma_{e,\text{max}}^{s-2} \right]^{1/(s-1)} & \text{if } 1 < s < 2, \\ \frac{p}{\rho} \frac{\epsilon_e}{\zeta_e} \frac{m_p}{m_e c^2 (\hat{\gamma}-1)} \left[\ln \left(\frac{\gamma_{e,\text{max}}}{\gamma_{e,\text{min}}} \right) \right]^{-1} & \text{if } s = 2. \end{cases} \quad (8)$$

For the upper electron Lorentz factor we used a constant fraction of the lower electron Lorentz factor, namely

$$\gamma_{e,\text{max}} = \epsilon_\gamma \gamma_{e,\text{min}}. \quad (9)$$

The normalisation coefficient of the non-thermal particle distribution can be obtained by performing the integral in Eq. (6) within the boundaries given by $\gamma_{e,\text{min}}$ and $\gamma_{e,\text{max}}$, yielding

$$n_0 = \frac{\epsilon_e p (s-2)}{(\hat{\gamma}-1) \gamma_{e,\text{min}}^2 m_e c^2} \left[1 - \left(\frac{\gamma_{e,\text{max}}}{\gamma_{e,\text{min}}} \right)^{2-s} \right]^{-1}. \quad (10)$$

Since the information on the magnetic field cannot be obtained from our purely hydrodynamical numerical simulations, we introduce it through its fraction ϵ_B of the equipartition magnetic field, namely, we set

$$B = \sqrt{8\pi \epsilon_B \frac{p}{\hat{\gamma}-1}}. \quad (11)$$

Following Mimica et al. (2009), the emission and absorption coefficients for the non-thermal emission, respectively $\epsilon_{\nu,\text{nt}}$ and

$\alpha_{\nu,\text{nt}}$, may be written as¹

$$\epsilon_{\nu,\text{nt}} = C n_0 \gamma_{e,\text{min}}^s \int_{\gamma_{e,\text{min}}}^{\gamma_{e,\text{max}}} \gamma_e^{-s} H\left(\frac{\nu}{\nu_0 \gamma_e^2}\right) d\gamma_e, \quad (12)$$

$$\alpha_{\nu,\text{nt}} = C n_0 \frac{p+2}{m_e \nu^2} \gamma_{e,\text{min}}^s \int_{\gamma_{e,\text{min}}}^{\gamma_{e,\text{max}}} \gamma_e^{-(s+1)} H\left(\frac{\nu}{\nu_0 \gamma_e^2}\right) d\gamma_e, \quad (13)$$

where the characteristic frequency, $\nu_0 = 3eB \sin \theta / (4\pi m_e c)$ with θ the angle between the direction to the observer and the direction of the magnetic field, $C = \sqrt{3} e^3 B \sin \theta / (8\pi m_e c^2)$, and e is the electron charge.

The value of $H(\xi)$ depends on the orientation of the magnetic field: If the magnetic field is ordered, $H(\xi) = F(\xi)$:

$$F(\xi) = x \int_x^\infty d\xi K_{5/3}(\xi), \quad (14)$$

where $K_{5/3}$ is the modified Bessel function of the second kind of order 5/3; in the case of a random magnetic field $H(\xi) = R(\xi)$, so that

$$R(\xi) = \frac{1}{2} \int_0^\pi d\alpha \sin^2 \alpha F\left(\frac{x}{\sin \alpha}\right), \quad (15)$$

with α the angle between the comoving magnetic field and the line of sight. For the functions $F(\xi)$ and $R(\xi)$ we used the approximations given by [Crusius & Schlickeiser \(1986\)](#) and [Joshi & Böttcher \(2011\)](#), namely

$$F(\xi) = 1.800151957 \xi^{0.304526404} e^{-\xi}, \quad (16)$$

$$R(\xi) = \begin{cases} 1.4980728 \xi^{1/3}, & \text{for } \xi < 0.01 \\ 1.08895 \xi^{0.20949} e^{-\xi} - \\ 0.00235861 \xi^{-0.79051} e^{-\xi}, & \text{for } \xi > 0.01 \end{cases} \quad (17)$$

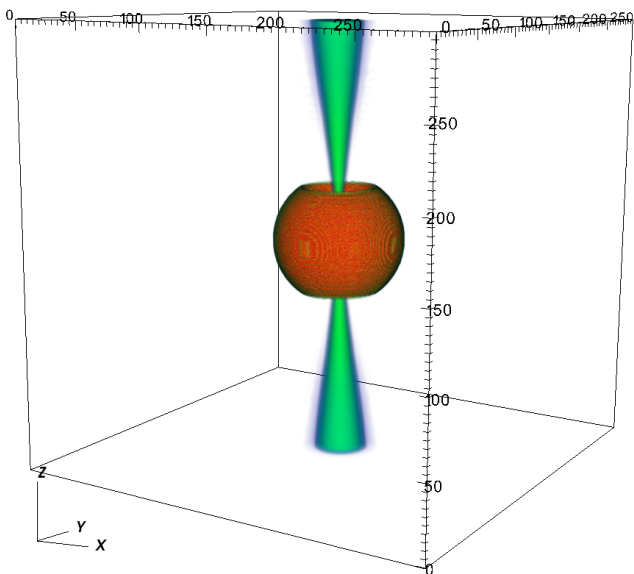


Fig. 6. Example of the 3D geometry of the jet-torus model

¹ We used unprimed variables for the co-moving frame and primed variables for the observer frame.

In order to compute the observed emission, we transformed the coefficients of emission $\epsilon_{\nu,\text{nt}}$ and absorption $\alpha_{\nu,\text{nt}}$, into the observer's frame and corrected for cosmological effects

$$\epsilon'_{\nu,\text{nt}} = D^{2+(p-1)/2} (1+z)^{-(p-1)/2} \epsilon_{\nu,\text{nt}}, \quad (18)$$

$$\alpha'_{\nu,\text{nt}} = D^{(p-1)/2+5/2} (1+z)^{-(p-1)/2-5/2} \alpha_{\nu,\text{nt}}, \quad (19)$$

where the Doppler factor is defined as $D := \Gamma^{-1} (1 - v_b \cos \vartheta)^{-1}$ and z denotes the redshift.

In addition to the non-thermal component, the emission includes also the contribution from a dusty torus, so that the thermal absorption coefficient $\alpha_{\nu,\text{th}}$ is given by

$$\alpha_{\nu,\text{th}} = 3.7 \times 10^8 T^{-1/2} Z^2 \frac{\rho^2}{m_p^2} \nu^{-3} (1 - e^{h\nu/k_b T}) \bar{g}_{\text{ff}}, \quad (20)$$

where $Z = \mu_i / \mu_e$ with $\mu_e = 2/(1+X)$ and $\mu_i = 4/(1+3X)$ where X corresponds to the abundance of hydrogen (set here to be $X = 0.71$) and \bar{g}_{ff} is the velocity-averaged gaunt factor (see, e.g., [Rybicki & Lightman 1986](#)). For the gaunt factor we used the values tabulated by [van Hoof et al. \(2014\)](#) and applied a bilinear interpolation in $\log u - \log \gamma^2$ space, where $u = (h\nu)/(k_b T)$ and $\gamma^2 = (Z^2 \text{Ry})/(k_b T)$, and Ry is the Rydberg energy.

The total intensity, I_ν , was a mixture of the non-thermal emission/absorption and thermal absorption (if the ray propagated through the dusty torus) and was computed via the transport equation as

$$\frac{dI_\nu}{ds} = \epsilon_{\nu,\text{nt}} - (\alpha_{\nu,\text{nt}} + \alpha_{\nu,\text{th}}) I_\nu, \quad (21)$$

where ds is the path length along a ray. For the calculation of the emission we computed the starting point of each ray at the position where the optical depth $\tau = \tau_{\text{limit}}$ and followed the ray to the observer. The optical depth is defined as

$$\tau = \int_0^{s'} (\alpha_{\nu,\text{nt}} + \alpha_{\nu,\text{th}}) ds. \quad (22)$$

The observed flux density can be computed from the intensity according to

$$S_\nu = \left(\frac{1+z}{D_L^2} \right) \Delta x \Delta y I_\nu, \quad (23)$$

where D_L is the luminosity distance, Δx and Δy represent the resolution of the detector's frame. The luminosity distance is computed via the equation provided by [Pen \(1999\)](#), where we took $\Omega_m = 0.27$ and a Hubble constant of $H_0 = 71 \text{ km s}^{-1} \text{ Mpc}^{-1}$. The final jet-torus geometry at a viewing angle of $\vartheta = 0^\circ$ used for the calculation of the emission is shown in [Fig. 6](#); furthermore, hereafter we assume ($D_L = 21.1 \text{ Mpc}$), which corresponds to a redshift of $z = 0.005$.

3.3. Parameter space study

In this Section we analyse the influence of the emission and torus parameters on the observed spectrum. In [Table 2](#) we provide an overview of the parameters used and of the values for our reference model. Quite generically, such parameters can be divided into three classes: i) "scaling parameters", ii) "emission parameters", and iii) "torus parameters"; we will discuss them separately below.

In order to cover a wide frequency range, i.e., $10^9 \text{ Hz} < \nu < 10^{12} \text{ Hz}$, we used a logarithmic grid with 100 frequency bins.

Table 2. Parameters for the emission simulations and values for the reference model

Symbol	Value	Description
\bar{d}_k	1.0	pressure mismatch at nozzle
n	1.5	pressure gradient in ambient medium
m	2.0	pressure gradient in ambient medium
z	0.005	redshift
R_j	3×10^{16} cm	jet radius
ρ_a	1.67×10^{-21} g cm $^{-3}$	ambient medium density
ϵ_B	0.1	equipartition ratio
ϵ_e	0.3	thermal to non-thermal energy ratio
ζ_e	1.0	thermal to non-thermal number density ratio
ϵ_γ	1000	ratio between e $^-$ Lorentz factors
s	2.2	spectral index
ϑ	80 $^\circ$	viewing angle
L_{AGN}	1×10^{43} erg s $^{-1}$	bolometric luminosity
R_{out}	3×10^{17} cm	torus outer radius
θ	50 $^\circ$	torus thickness
$\rho(R_{\text{in}})$	1.67×10^{-19} g cm $^{-3}$	torus density at R_{min}
T_{sub}	1500 K	dust sublimation temperature
k, l	1, 2	exponents for ρ and T distributions

The ray-tracing was performed using a Delaunay triangulation on the axisymmetric RHD simulations with (r, z) coordinates to a 3D Cartesian grid (x, y, z) with a typical resolution of 300^3 cells (see Fig. 6 for a 3D representation of the jet-torus system).

3.3.1. Single-dish spectra

To demonstrate the influence of the torus on the spectrum we computed the emission for the reference model with and without a torus. The result of these calculations is presented in Fig. 7, where the black lines indicate simulations including a torus, while red lines are used for simulations without a torus. Furthermore, solid lines refer to the total flux density, while dashed and dotted lines correspond to the emission from the jet and from the counter-jet, respectively.

Not surprisingly, in the low-frequency regime, i.e., for $\nu < 10^{11}$ Hz, simulations with a torus show a smaller flux than simulations without a torus, simply as a result of the increased absorption along the line of sight. At higher frequencies, the flux densities of both simulations are very similar since the torus becomes optically thin at these frequencies. The comparison between the emission from the jet (dashed lines) and from the counter-jet (dotted lines) shows that the counter-jet is more affected by the absorption of the torus than the jet. This is to be contrasted with the results obtained in the case of simulations of jets with a torus, where the emission converges around $\nu \sim 10^{11}$ Hz to the flux density of the jet without torus. A similar behaviour was obtained for the counter-jet but at a higher frequency, i.e., $\nu \sim 3 \times 10^{11}$ Hz.

Figure 8 shows the single-dish spectrum for the different jet-torus and ambient medium models (see Table 1). Within the same ambient medium, the PM jets ($d_k = 1$, dashed lines in Fig. 8) exhibits higher flux densities than the OP jets ($d_k = 2.5$, solid lines in Fig. 8). Furthermore, OP jets show a flatter spectrum than PM jets within $10^9 \text{ Hz} \leq \nu \leq 10^{11} \text{ Hz}$. The general trend could be described as follows: the steeper the gradient in the ambient medium, the flatter the spectrum. The change in the spectral slope at $\nu \sim 10^{11}$ Hz is indicative of the turnover frequency of the torus, i.e., the frequency at which the torus becomes optically thin (see also Fig. 7).

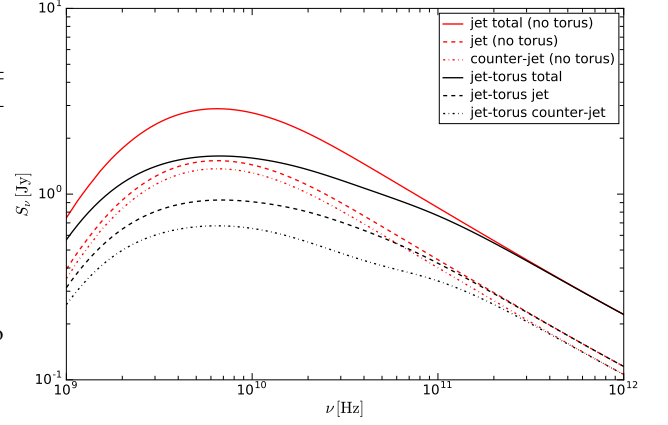
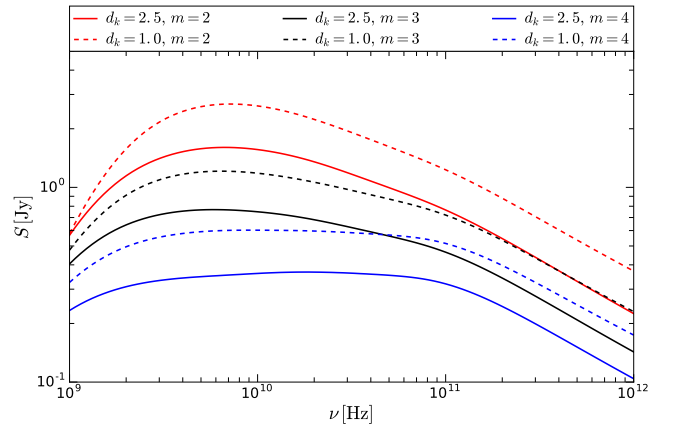
**Fig. 7.** Single-dish spectra for a simulation including a torus (black) and without a torus (red).**Fig. 8.** Single-dish spectra for the different jet and ambient medium models.

Figure 9 is meant to summarise the impact of the different scaling parameters, R_j , ϑ , and, L_{kin} , on the single-dish spectrum. More specifically, we have computed the emission when only one of the scaling parameters is varied while the others are kept fixed to the values listed in Table 2. The variation in the observed flux can then be summarised as follows:

- *Jet radius, R_j* : The jet radius acts as the scaling length of the simulations and has the largest impact on the observed single-dish spectrum (see panel a in Fig. 9). The increase in flux with R_j follows a simple scaling $\sim \Delta R_j^2$, as expected from Eq. (23).
- *Viewing angle, ϑ* : Due to Doppler boosting, the observed spectrum is shifted towards higher flux densities and higher turnover frequencies with decreasing viewing angle. Since we use large viewing angles for our simulations the variations in the spectrum are minor.
- *Bolometric luminosity, L_{kin}* : Changes in the bolometric luminosity lead to a variation in the inner radius of the torus [cf., Eq. (2)]. Lowering the kinetic luminosity decreases the inner radius of the torus. Since we keep the outer radius of the torus fixed, the total size of the torus increases with decreasing kinetic luminosity and smaller values for rest-mass density and temperature are obtained. Since the opacity of the torus scales like $\tau_{\text{torus}} \propto T^{-1/2} \rho^2$ (when assuming T and ρ to decay as r^{-k}), lower densities lead to lower opacities and

a large emission from the jet. As a result, the observed flux density increases with decreasing kinetic luminosity.

In Fig. 10 we report the effect of the emission parameters ϵ_e , ϵ_b , ζ_e , ϵ_γ , and s on the observed single-dish spectrum while keeping the other parameters fixed. The emission simulations were performed using our reference model (see Table 2).

- *Ambient medium rest-mass density, ρ_a* : A variation in the ambient medium rest-mass density ρ_a leads to large changes in the shape and the total flux density of the spectrum (see panel a in Fig. 10). The single-dish spectrum steepens and is shifted to higher turnover flux densities with increasing ambient medium rest-mass density.
- *Thermal to non-thermal energy ratio, ϵ_e* : If more energy is stored in the non-thermal particles via an increase in ϵ_e , the turnover frequency increases, while the turnover flux density rises only slightly. The spectral index within $\nu \sim 10^{11}$ Hz decreases in absolute values, thus leading to a flatter spectrum (see panel b in Fig. 10).
- *Equipartition ratio, ϵ_b* : An increase of the equipartition fraction ϵ_b leads to higher observed flux densities on the single-dish spectrum and to a shift of the turnover position towards smaller frequencies and higher flux densities (see panel c of Fig. 10). Additionally, the spectrum steepens for $\nu < 10^{11}$ Hz.
- *Ratio between thermal to non-thermal number densities, ζ_e* : Increasing the number of non-thermal particles leads to higher observed flux densities and shifted the turnover frequency towards lower frequencies. Additionally, the spectral slope increases (see panel d of Fig. 10).
- *Ratio between upper and lower e^- -Lorentz factors, ϵ_γ* : The variation of ϵ_γ had only a minor effect on the single-dish spectrum (see panel e in Fig. 10). An increase in γ_{\max} leads to a flattening of the spectrum at high frequencies ($\nu > 10^{11}$ Hz) and shifted the high-frequency cut-off in the spectrum towards higher frequencies, which are clearly visible for $\gamma_e = 10^2$ (see blue line in panel e).
- *Spectral slope, s* : Changing the spectral slope of the non-thermal particle distribution induced only minor variations in the observed flux densities. However, the slope of the spectrum for $\nu \leq 10^{11}$ Hz flattens, while for $\nu > 10^{11}$ Hz the spectral slope steepens with increasing s (see panel f in Fig. 10).

Since the properties of the obscuring torus strongly affect the observed emission, we have also performed a parameter-space study varying the torus' properties reported in Table 2. We recall that in our model the torus is characterised by its geometry (R_{out} and Θ) and by the distribution of the rest-mass density and the temperature [see Eqs. (3)–(4)]. The first row in Fig. 11 summarises the changes on the single-dish spectrum result from the torus geometry, while the second row shows the modification in the spectral shape depending on the distribution of the rest-mass density and temperature. Overall, the variations in the spectrum can be summarised as

- *Torus geometry*: The variation of the torus geometry and its effect on the single-dish spectrum is presented in the top row of Fig. 11. From left to right we show the effects of the torus outer radius, R_{out} , the torus thickness, Θ , and the torus rest-mass density, ρ_t . Increasing the outer radius of the torus leads to a drop in the observed emission between $10^9 \text{ Hz} \leq \nu \leq 10^{11} \text{ Hz}$. The influence of the torus thickness is presented in panel b of Fig. 11, which shows that the observed flux density decreases as the thickness of the torus is increased.

- *Density distribution*: The observed flux density decreases with increasing torus rest-mass density. At the same time, the turnover frequency is shifted towards higher frequencies (see panel d in Fig. 11).
- *Temperature distribution*: Variations in the torus' temperature have only minor impacts on the observed flux density, so that the hotter the torus the higher the observed flux density (see panel g in Fig. 11).
- *Radial and angular distribution of the torus rest-mass density and torus temperature*: The gradient in the radial direction modifies mainly the total observed flux density, with a steeper gradient in the radial direction leading to an increase in the flux density (see panel e in Fig. 11). On the other hand, a larger effect on the shape of the spectrum comes from changing the gradient in the polar direction (see panel f). More specifically, if the temperature distribution is more concentrated at the edges and the rest-mass density falls off more rapidly towards the edges of the torus (i.e., if larger values for l are used), the spectrum steepens and the observed flux density is higher than for smoother rest-mass density and temperature distributions (i.e., for smaller values for l).

All things considered, the parameter study on the single-dish spectrum can be summarised as follows: The scaling parameter R_j and the ambient medium rest-mass density ρ_a have the largest impact on the observed single-dish flux density (see panel a in Fig. 9 and Fig. 10). Changes in the emission parameters, ϵ_e , ϵ_b , ζ_e , ϵ_γ , and s mainly modify the shape of the spectrum and lead only to minor variations in the flux density (see Fig. 10). The torus parameters show the smallest effect and alter mainly the slope in the optically thin regime of the spectrum (see Fig. 11).

3.3.2. Synthetic radio maps

To facilitate comparison with VLBI observations, we computed radio maps at different frequencies and convolved them with a 2D Gaussian beam. The size of the beam depends on the properties of the array and on the observing frequency. In Table 3 we present the typical beam sizes (uniform weighting, full-track (u, v) coverage for a source at -8° declination) for the Very Long Baseline Array (VLBA) and its sensitivity, i.e., the lowest detectable thermal noise (see the EVN calculator² for details). If not stated otherwise, a flux-density cut off of $5 \times S_{\text{limit}}$ was used for the synthetic radio maps.

Table 3. VLBA properties used for the convolution of the radio maps.

ν [GHz]	b_{maj} [mas]	b_{min} [mas]	S_{limit} [μJ]
5	3.30	1.30	22
8	1.98	0.81	27
15	1.28	0.50	43
22	0.86	0.32	50
43	0.45	0.16	93
86	0.35	0.06	421

In Fig. 12 we show the convolved radio maps at 15 GHz for different ambient medium and jet models (similar to Fig. 4). The panels show, from top to bottom, different models for the ambient medium and in each panel the upper half (i.e., $(0-1) \times 10^{18} \text{ cm}$

² <http://www.evlbi.org/cgi-bin/EVNcalc>

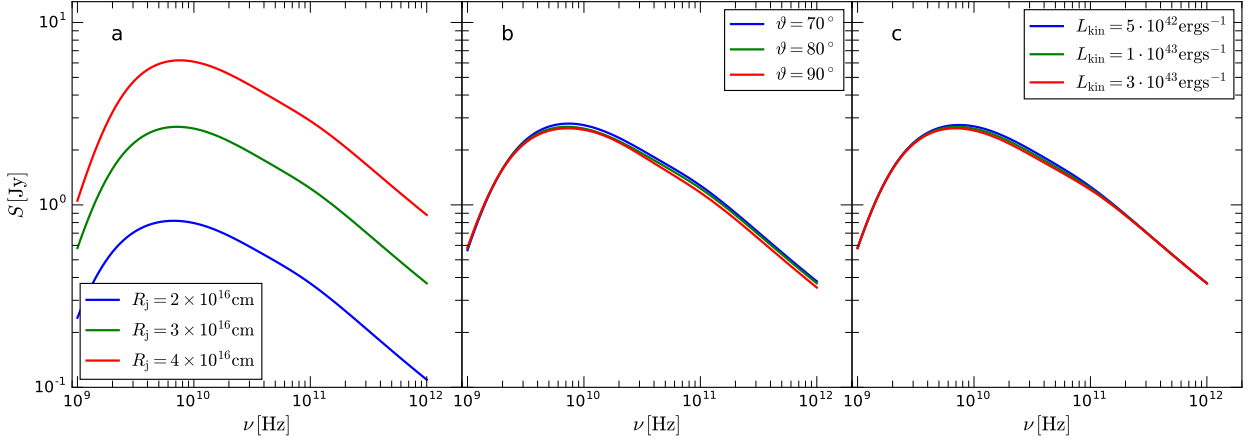


Fig. 9. Influence of the scaling parameters R_j , ϑ and L_{kin} on the shape of the observed single-dish spectrum

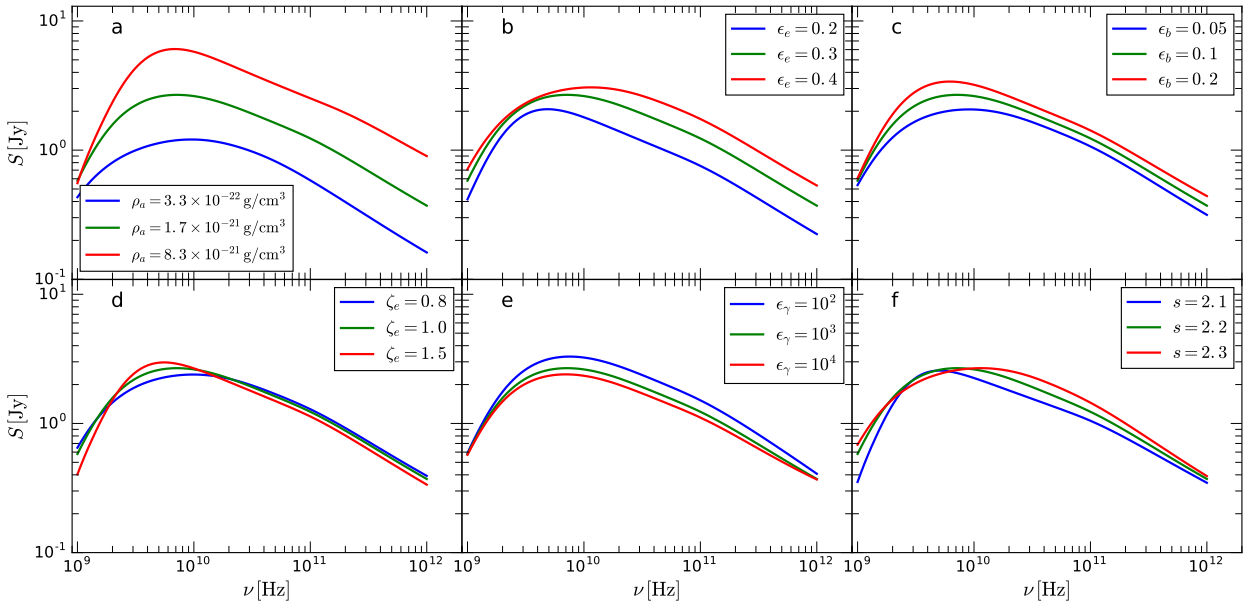


Fig. 10. Influence of the emission parameters ρ_a , ϵ_e , ϵ_b , ζ_e , ϵ_γ , and s on the shape of the observed single-dish spectrum.

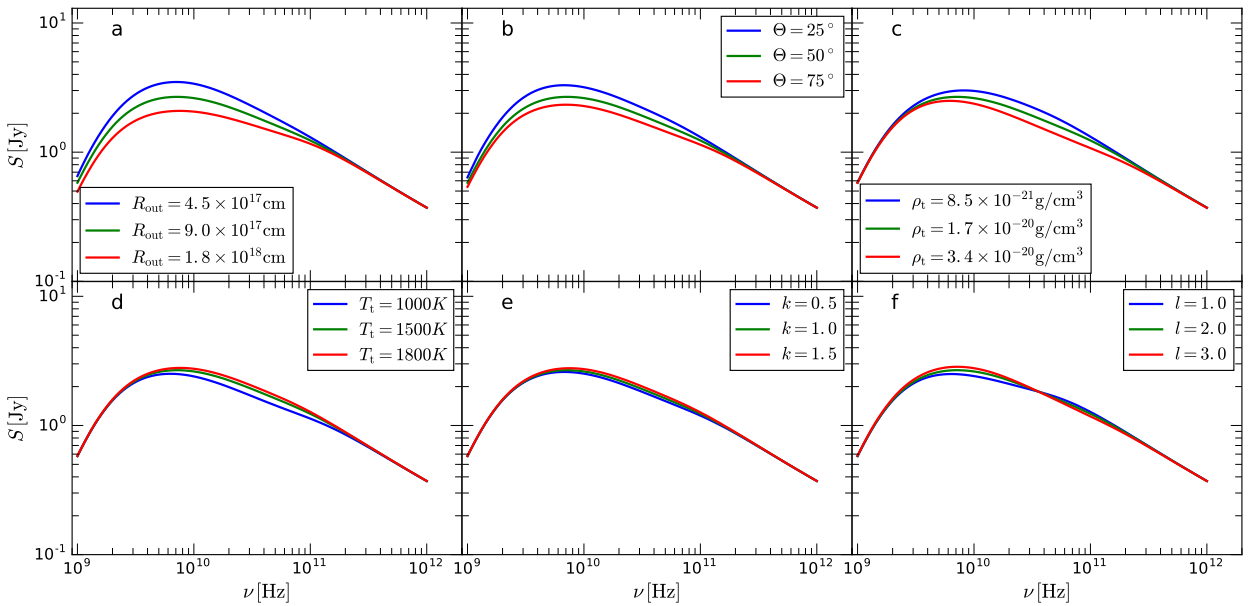


Fig. 11. Influence of the torus parameter on the observed single-dish spectrum. Top row from left to right: torus outer radius, torus thickness and torus rest-mass density. Bottom row from left to right: torus temperature, the distribution of the torus rest-mass density, and the distribution of the torus temperature

corresponds to the OP jet and lower half (i.e., $(-1-0) \times 10^{18}$ cm) to the PM jet. The width of the jet increases with the gradient in the ambient medium, from top to bottom, from 0.5×10^{18} cm to 0.8×10^{18} cm, while the observed flux density decreases. Within a common atmosphere, the OP jets (upper half of each panel) show a less elongated core region as compared to the PM jets (lower half of each panel) and the axial flux density decreases faster in OP jets than in PM jets. These effects become more visible as the rest-mass density gradient in the ambient medium is increased.

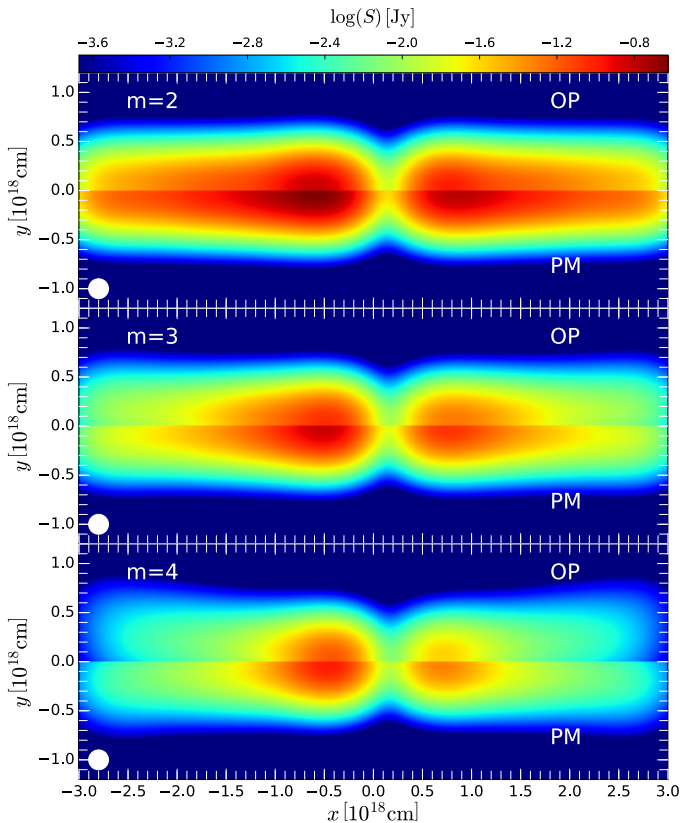


Fig. 12. Convolved radio maps at 15 GHz. The panels correspond to different gradients used in the ambient medium indicated by n and m . In each panel the upper half corresponds to an OP jet and the lower half to a PM jet. The convolving beam is plotted in lower left corner of each panel.

Analogous to the parameter study performed on the single-dish spectra (see Sec. 3.3.1), we have investigated the impact of the emission parameters presented in Table 2 on the synthetic radio maps. Figure 13 summarises the effects of the viewing angle ϑ , of the thermal to non-thermal energy ratio ϵ_e , and of the rest-mass density of the torus ρ_t , on the 15 GHz radio maps. For a better comparison, the reference model is included in the second row of Fig. 13.

At smaller viewing angles (i.e., for $\vartheta = 60^\circ$), the jets appear more asymmetric due to the increased Doppler boosting and larger opacity along the line of sight, especially for the counter-jet (see the top panel in the first row of Fig. 13). However, with increasing viewing angle the asymmetries between jet and counter-jet tend to disappear, while the total flux density in the radio map decreases. Upon varying the non-thermal to thermal energy ratio ϵ_e , the flux density increases and affects both jets in the same way (see second row in Fig. 13). On the other hand, a

change in ϵ_e does not alter the jet structure or the emission gap between the jet and the counter-jet.

In the third row of Fig. 13 we show the changes in the 15 GHz radio maps due to a variation in the torus rest-mass density, ρ_t . Since we keep the torus size constant, a change in the torus rest-mass density does not have an impact on the observed emission at $|x| > 1 \times 10^{18}$ cm. However, the observed gap between jet and counter-jet does change depending on the torus rest-mass density. In particular, the gap is nearly invisible at low densities (top panel in the third row) while it is clearly noticeable at higher densities (see last panel in the third row of Fig. 13). Besides the changes in the gap between the jet and counter-jet, a variation in the torus rest-mass densities leads to changes in the observed flux densities within $|x| < 1 \times 10^{18}$ cm. This can be easily explained as due to the increased opacity, which reduces the flux reaching the observer (see the decreasing flux density at $x = 0.5 \times 10^{18}$ cm).

In the analysis of VLBI observations it is common to compute spectral index maps, where the spectral index, α , between to adjacent frequencies ν_1 and ν_2 is given by

$$\alpha_{\nu_1, \nu_2} := \frac{\log(S_{\nu_1}/S_{\nu_2})}{\log(\nu_1/\nu_2)}. \quad (24)$$

To avoid resolution-induced artefacts in the spectral index maps, a common beam size was used for the convolution. Furthermore, as is usually done in observational VLBI in order to avoid over-resolution from the high-frequency image, the beam size was set on the low-frequency map.

In Fig. 14 we present the spectral index computed between 22 GHz and 43 GHz for different torus densities indicated in the top left corner. The spectral index (SPIX) is found to be negative (i.e., $\alpha \sim -0.6$) for regions $|x| > 0.5 \times 10^{18}$ cm to reflect optically thin regions, and positive (i.e., $\alpha \sim 2.5$) for $|x| < 0.5 \times 10^{18}$ cm to reflect optically thick jet regions.

These inner regions absorb a large fraction of the emission due to the high rest-mass density in the surrounding torus. Indeed, as the torus rest-mass density is increased, more emission is found to be absorbed and the optically thick region expands towards the edges of the torus (compare the top to the bottom panels in Fig. 14). Besides the expansion of the optically thick region, the spectral index also generally increases for larger torus rest-mass densities. Thus, the extent of the optically thick region and the value of the spectral index can be used to deduce the size and the rest-mass density of the obscuring torus.

Multifrequency VLBI observations enable us to investigate the opacity and therefore the frequency-dependent position of the so-called “radio core”, i.e., of the first detectable flux-density maximum. The variation of this position with frequency provides details of the rest-mass density and the magnetic field in the source. This effect is called “core-shift” (see Lobanov 1998, for details). In VLBI observations the initial position of the jet is lost during the imaging process and different techniques are used to reconstruct the core-shift between adjacent frequencies (see Fromm et al. 2013b, for a summary). However, this is not needed when working with synthetic radio maps, since the initial position is known. Here, we define the core as the position of the first flux-density maximum along an axial slice through the convolved radio map.

In Fig. 15 we present multifrequency VLBI radio maps from 8 GHz to 86 GHz based on our reference model (see Table 2 for the parameters used). The total flux density of the radio maps and the transversal size of the jets decreased with frequency, where the latter could be explained by the convolution with the observing beam (see Table 3). Given the parameters used for our

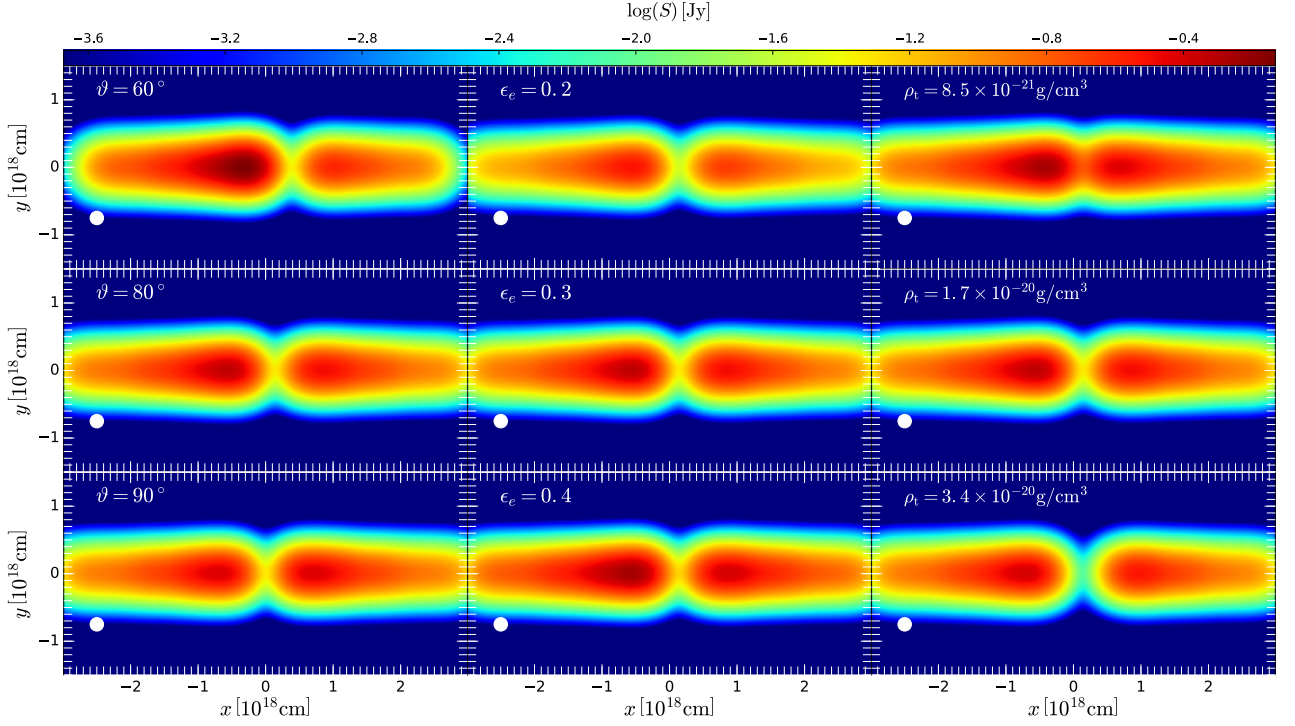


Fig. 13. Influence of the viewing angle (left column), the thermal to non-thermal energy ratio (middle column) and the torus rest-mass density (right column) on the 15 GHz radio maps. The convolving beam is plotted in the lower left corner of each panel.

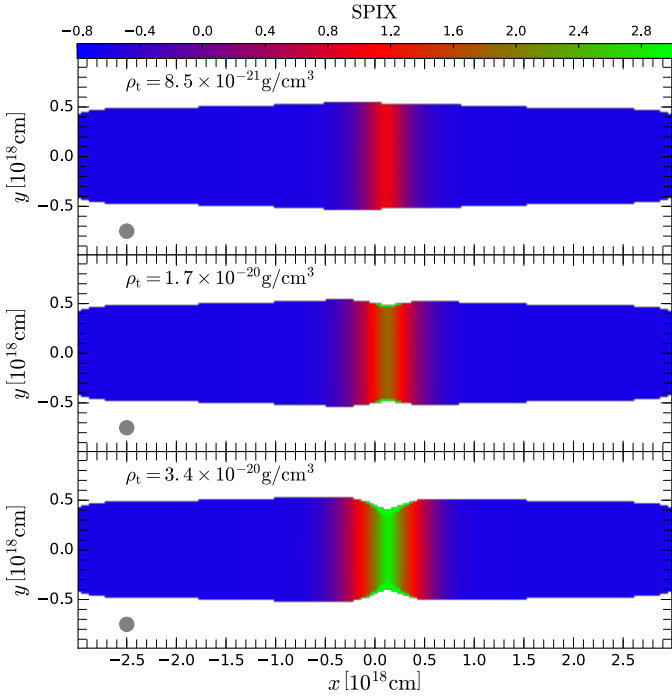


Fig. 14. Spectral index maps computed between 22 GHz and 43 GHz for different torus densities. The convolving beam is plotted in the lower left corner of each panel.

reference model, the turnover frequency is at ~ 8 GHz, so that the flux density decreases as $S_\nu \propto \nu^{-(s-1)/2}$ for $\nu > 8$ GHz. Since the flux density is smaller at higher frequencies and the sensitivity of the array also decreases with frequency (see third column of Table 3), the jets appear shorter in size at higher frequencies. Furthermore, besides a drop in the observed emission with fre-

quency, the gap between the jet and counter-jet is reduced with frequency and the position of the flux-density maximum in the jet and the counter-jet is shifted upstream.

In Fig. 16 we present the core-shift obtained from the synthetic multifrequency radio maps shown in Fig. 15. The red stars correspond to the position of the radio core in the counter-jet and the blue stars to the position of the radio core in the jet. The inset panel in Fig. 16 shows a magnified view of the nozzle region of the jets and the symbols indicate the position of the core. As mentioned previously, the core positions in the jet and counter-jet shift upstream with frequency; at the same time, however, the amount of the shift differs between the jet and counter-jet. This behaviour could be explained in terms of the different amounts of absorption along the line of sight for rays crossing the obscuring torus. The opacity is clearly larger for rays emerging from the counter-jet since they have to cross the entire torus, in contrast to rays from the jet and which need to cross only a fraction of the torus. At $\nu \sim 80$ GHz, the torus becomes optically thin and both cores are shifted towards the footpoint of the jets (here at $x = 0$).

Also reported in Fig. 16 are the core-shifts obtained from an OP jet (diamond markers). The computed core-shifts show the same behaviour as the PM jet for $\nu < 20$ GHz. For larger frequencies, both the jet and counter-jet show a plateau occurring between $\nu \sim 20$ GHz and $\nu \sim 70$ GHz. In this frequency range, the recollimation shocks in the jets mimic the radio core (i.e., they produce a local flux-density maximum) and since their position is frequency-independent, the core-shift does not decrease with frequency. On the other hand, if the observing frequency is increased, the upstream emission of the recollimation shocks becomes optically thin and a new flux-density maximum is produced further upstream. Similar to the PM jet, the torus becomes optically thin around $\nu \sim 80$ GHz and the core positions converge towards the footpoint of the jet.

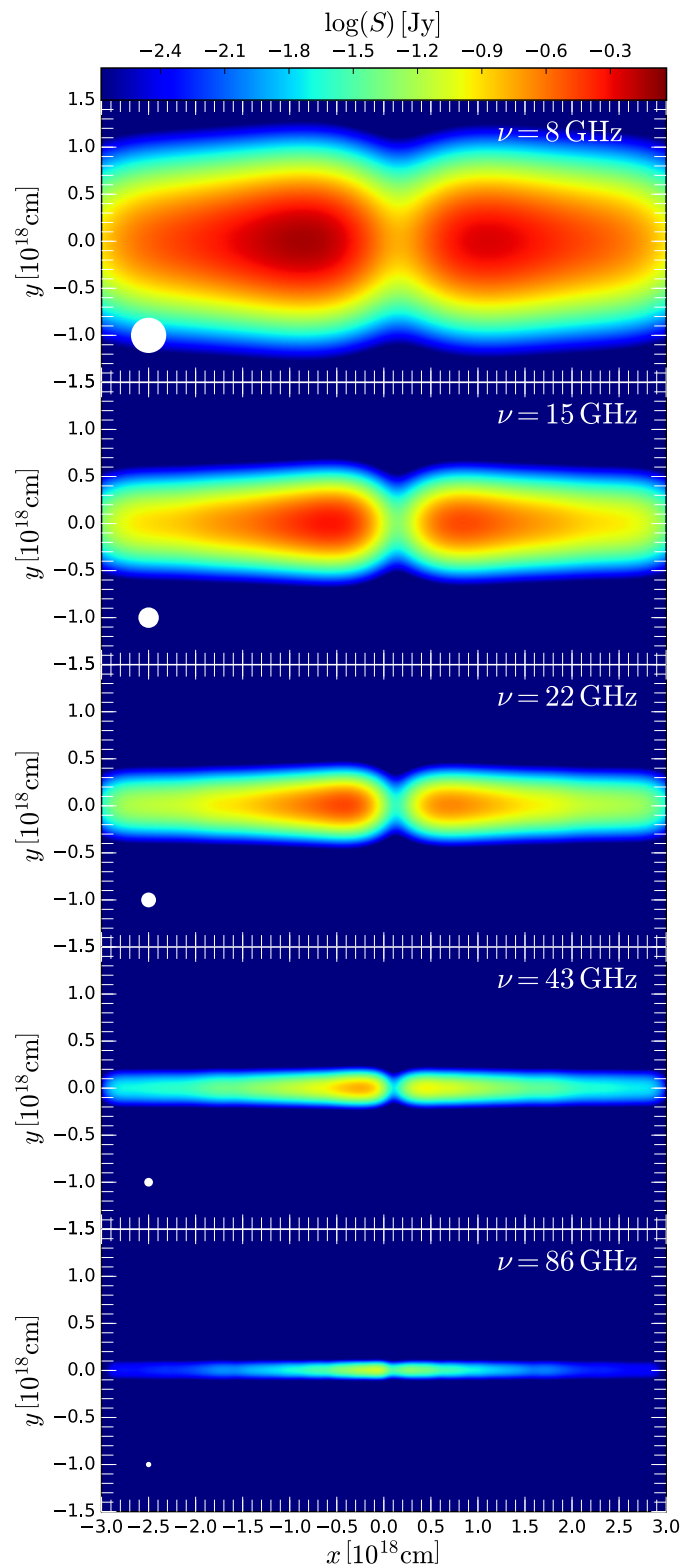


Fig. 15. Synthetic multifrequency radio maps from 8 GHz to 86 GHz. The convolving beam is plotted in the lower left corner of each panel.

4. Summary and outlook

We investigated the connection between jets in an ambient medium of decreasing pressure surrounded by a stationary torus. We then simulated jets using the state-of-the-art RHD code

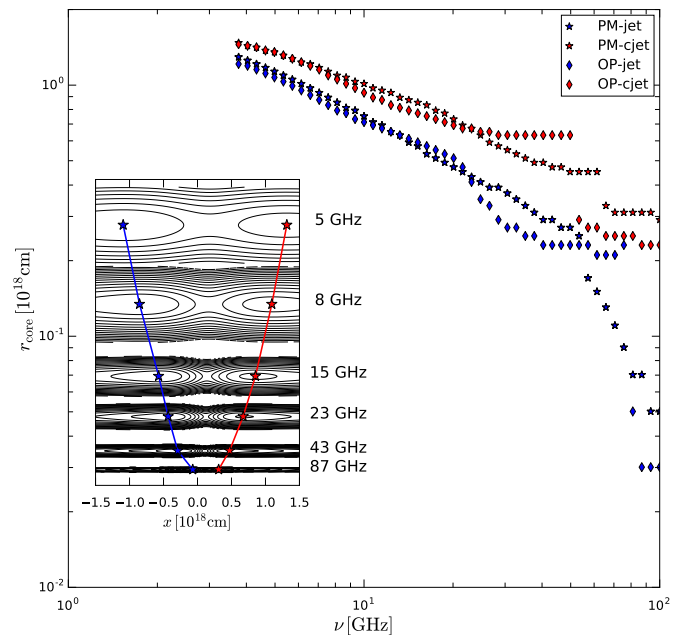


Fig. 16. Variation of the core-shift with frequency as obtained from our reference model. The inset panel shows a contour plot of the synthetic radio maps over-plotted with corresponding core position for different observing frequencies.

Ratpenat (Perucho et al. 2010) and included a stationary torus. The properties of the torus were motivated by both observations and theoretical modelling. In the post-processing we used a newly developed emission code and computed the thermal and non-thermal emission. To investigate the effect of the scaling parameters on the observed emission (single-dish spectra and multifrequency radio maps) we performed a detailed parameter study and produced observable signatures which can be used to distinguish between different jet, ambient medium and torus configurations based on single dish and VLBI observations. We applied a core-shift analysis to the synthetic radio maps produced and demonstrated how one can distinguish between OP jets and PM jets depending on the slope of the core-shift. Our simulations and the extensive analysis of the parameter space study have shown that the observed emission is the result of a delicate interplay between hydrodynamical effects and emission and absorption processes.

A particularly robust result of this analysis is that the observed spectra of PM jets exhibit higher flux densities than the spectra of OP jets. This is due to the fact that because of the initial pressure mismatch at the jet nozzle, the OP jets expand faster and convert internal energy into kinetic energy more efficiently than PM jets. At large viewing angles, the emission is strongly de-boosted for faster jets and, as a result, less emission is received by the observer. Also, while the spectra alone make it difficult to distinguish these two types of jets, high-frequency radio maps show a clear difference in both the morphology of the jet and in the evolution of the flux density along the jet. More specifically, OP jets exhibit local maxima in the flux density at the position of the recollimation shocks; on the other hand, in PM jet the flux density decreases continuously along the jet axis (Gómez et al. 1997; Mimica et al. 2009; Fromm et al. 2016).

Another important result of our analysis is that the inclusion of a stationary torus in the synthetic emission consistently

leads to a strong absorption in the single-dish spectrum. This behaviour is mostly due to the enhanced rest-mass density between the jet and the observer, which in turn increases the opacity along the line of sight. Additionally, depending on properties of the torus, the spectrum flattens within a certain frequency range. Overall, the geometry of the torus has the greatest influence on the observed spectrum. In particular, increasing the geometrical size of the torus leads to a longer path for the rays generated in the jets, which then pass through a high rest-mass density field, thereby increasing the opacity along the line of sight. Indeed, if the torus is large enough and its rest-mass density sufficiently high, it can block a considerable fraction of the jet, which then becomes invisible to an observer. This effect is reflected in the flattening of the spectrum, in the appearance of an emission gap between the jet and counter-jet in the synthetic radio maps, and in optically thick spectral-index maps. We note that since the thermal absorption coefficient scales like ν^{-3} , the aforementioned effects are frequency-dependent, i.e., the spectra including a torus should converge to the one without a torus for $\nu > 10^{11}$ Hz, with the emission gap between the jet and the counter-jet vanishing with increasing frequency. Observationally, therefore, the spectral break could be used to constrain the rest-mass density within the torus. Given a dense frequency sampling, for example like that used in the FGamma program (Fuhrmann et al. 2016), the rest-mass density of the torus together with additional emission parameters can in principle be fitted.

This behaviour and in particular the frequency dependence on the spectral properties can be used to distinguish between OP and PM jets. In particular, since the gap is frequency-dependent, the observed onset of the jet and counter-jet is varying with frequency. At low frequencies the torus should block the observer's view and the onset of the jets are separated by an emission gap; at such frequencies, OP and PM jets are indistinguishable. However, at higher observing frequencies the gap between the jets will decrease, exposing the differences in the two types of jets. Since one of the key features of OP jets are recollimation shocks, which lead to local maxima in the pressure and rest-mass density along the jet, their presence will become visible as a local enhancement of the emission. At a certain frequency, the onset of the jet will coincide with the position of a recollimation shock, which itself is frequency independent and will not change until the upstream region becomes optically thinner and brighter than the recollimation shock. This effect will lead to the formation of plateaus in the core-shift plot. Because the behaviour described above is absent in the case of PM jets, for which no strong recollimation shocks are formed and no plateaus in the core-shift occur, observations should be able to provide information to discriminate between these two basic classes of jets. More specifically, using multifrequency VLBI observations, the size of the torus can be estimated by the dimensions of the optically thick region in the spectral index maps. The frequency-dependent size of the emission gap can be used to obtain estimates of the rest-mass density of the torus and analysis of the core-shift would enable one to differentiate between OP and PM jets.

In a follow-up paper we will apply the techniques presented here to actual observational data and include the propagation of shock waves using the so-called “slow-light” approach, which will enable us to investigate the temporal variations in the single-dish spectra and multifrequency radio maps.

Acknowledgements. Support comes from the ERC Synergy Grant “BlackHoleCam - Imaging the Event Horizon of Black Holes” (Grant 610058). MP acknowledges support by the Spanish “Ministerio de Economía y Competitividad” grants AYA2013-48226-C3-2-P and AYA2015-66899-P.

ZY acknowledges support from an Alexander von Humboldt Fellowship. ER acknowledges support from the grants AYA-2012-38491-C02-01, AYA2015-63939-C2-2-P, and PROMETEOII/2014/057. CMF wants to thank Walter Alef and Helge Rottmann for support during the computation on the MPIfR cluster and Mariafelicia De Laurentis and Hector Olivares for fruitful discussion and helpful comments to the manuscript.

Appendix

We performed a convergence test for our emission calculations and the results are presented in Fig. 17. For the test we used the same initial setup and increased the number of cells used in the computation in 100^3 steps. In Fig. 17 we show the single-dish spectrum between 1 GHz and 1 THz for different resolutions and the inset panel shows the variation of the total flux density with respect to the number of simulation grid cells. The calculated flux density converges to a common value and no significant differences were obtained above 400^3 cells. We note that at the lowest resolution (100^3) the high-frequency flux density is significantly different compared to the high resolution runs. This difference occurred since the high-frequency emission was created close to the jet nozzle and therefore emanates from a region of small transversal jet size. If the resolution was not sufficiently high to resolve these regions, the triangulation and interpolation of these cells onto the 3D grid failed (overestimating the contribution from the ambient medium) and led to unphysically small flux densities.

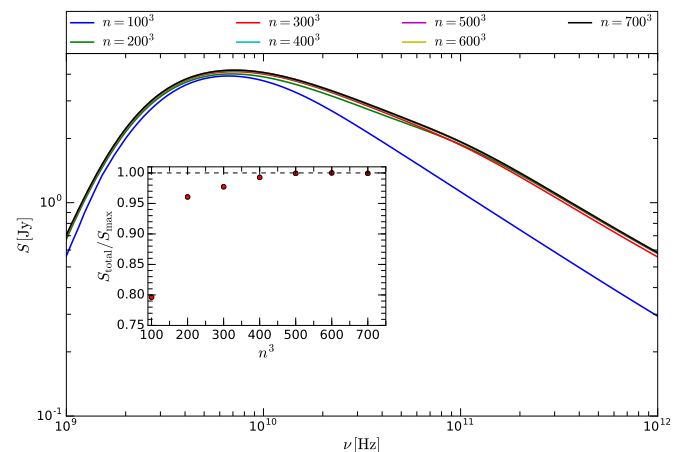


Fig. 17. Convergence test for the emission calculations. Single-dish spectrum for seven different resolutions.

References

- Antonucci, R. 1993, ARA&A, 31, 473
- Crusius, A. & Schlickeiser, R. 1986, A&A, 164, L16
- Daly, R. A. & Marscher, A. P. 1988, ApJ, 334, 539
- Falle, S. A. E. G. 1991, MNRAS, 250, 581
- Fanaroff, B. L. & Riley, J. M. 1974, MNRAS, 167, 31P
- Fromm, C. M., Perucho, M., Mimica, P., & Ros, E. 2016, A&A, 588, A101
- Fromm, C. M., Ros, E., Perucho, M., et al. 2013b, A&A, 557, A105
- Fuhrmann, L., Angelakis, E., Zensus, J. A., et al. 2016, ArXiv e-prints
- Gómez, J. L., Martí, J. M., Marscher, A. P., Ibanez, J. M., & Alberdi, A. 1997, ApJ, 482, L33
- Hardcastle, M. J. & Krause, M. G. H. 2013, MNRAS, 430, 174
- Hoenig, S. F. 2013, ArXiv e-prints
- Joshi, M. & Böttcher, M. 2011, ApJ, 727, 21
- Kharb, P., O’Dea, C. P., Baum, S. A., et al. 2008, ApJS, 174, 74
- Laing, R. A. & Bridle, A. H. 2002, MNRAS, 336, 328
- Lister, M. L., Aller, H. D., Aller, M. F., et al. 2009, AJ, 137, 3718

- Lobanov, A. P. 1998, *A&A*, 330, 79
- Mimica, P., Aloy, M. A., Agudo, I., et al. 2009, *ApJ*, 696, 1142
- Mizuno, Y., Gómez, J. L., Nishikawa, K.-I., et al. 2015, *ApJ*, 809, 38
- Pen, U.-L. 1999, *ApJS*, 120, 49
- Perucho, M. & Martí, J. M. 2007, *MNRAS*, 382, 526
- Perucho, M., Martí, J. M., Cela, J. M., et al. 2010, *A&A*, 519, A41
- Porth, O. & Komissarov, S. S. 2015, *MNRAS*, 452, 1089
- Rezzolla, L. & Zanotti, O. 2013, *Relativistic Hydrodynamics*
- Rybicki, G. B. & Lightman, A. P. 1986, *Radiative Processes in Astrophysics*, 400
- Schartmann, M., Meisenheimer, K., Camenzind, M., Wolf, S., & Henning, T. 2005, *A&A*, 437, 861
- Stalevski, M., Fritz, J., Baes, M., Nakos, T., & Popović, L. Č. 2012, *MNRAS*, 420, 2756
- Stalevski, M., Ricci, C., Ueda, Y., et al. 2016, *MNRAS*, 458, 2288
- Urry, C. M. & Padovani, P. 1995, *PASP*, 107, 803
- van Hoof, P. A. M., Williams, R. J. R., Volk, K., et al. 2014, *MNRAS*, 444, 420